A Theoretical and Experimental Study of Rock Cutting

M. C. Stavropoulou
Department of Geology
University of Athens, GR-15784 Athens, Greece

K. F. Giannakopoulos
GEMCO Engineering
89 Marathonodromon Str, GR-15452 Athens, Greece

G.E. Exadaktylos
Department of Mineral Resources Engineering
Technical University of Crete, GR-73100 Chania, Greece

1. SUMMARY

Two types of numerical models, namely a continuum and a micromechanical discrete element model, are employed for the theoretical study of rock cutting measurements by a new portable rotary microdrilling tool. Our objectives are: (a) to gain insight in the cutting mechanism of granular cohesive-frictional rocks, and (b) to examine the comparability of numerical model predictions with experimental results. In the first type of model, a plane strain continuum calculation is done with a non-hardening, elastic-plastic, Mohr-Coulomb material. In the second type of numerical model, distinct element calculations are done on a simulated plane strain sample of 540 discs. In both models measurements are made of components of traction applied to the cutting tool and compared with measurements taken with the acquisition system of the portable microdrilling tool during specially designed tests on Dionysos marble.

2. INTRODUCTION

Rock cutting experiments on different types of rocks used as monumental stones, such as marbles, limestones and sandstones with uniaxial compressive strengths ranging from 1 MPa to 110 MPa, were carried out within the framework of the EU (5^{th} Framework) funded Project DIAS /1/. These experiments were performed by using a new portable micro-drilling device that was first designed and constructed for the *in situ* evaluation of the hardness of stones (that is defined as the axial load on the cutter divided by the cross-sectional area of the cut) /2/. Subsequently, in a second phase of the tool development, the measurement of

torque during drilling was also provided by the manufacturer (SINT Technology srl, Via Giusti 229, Calenzano, Italy).

Despite the obvious advantages of the use of small size drilling to assess quickly and in a quasi-non-destructive manner the strength properties of rocks, the method has not become a standard investigation tool in stone and concrete industries, as well as in rock engineering practice. A major obstacle for this fact is the lack of appropriate back-analysis methodologies, since drilling measurements are affected by many parameters, such as size, geometry and material of the drill bit, friction between bit and geomaterial, heterogeneity, fabric, grain size, physico-chemical set-up of geomaterials to name a few. Nevertheless, the new portable microdrilling device should represent a potential method for the determination of mechanical properties of natural and artificial geomaterials, if the influence of the various test parameters are understood and controlled.

This paper deals with the numerical analysis of rock cutting experiments performed by this tool. The objective of this study is to establish whether or not results obtained in laboratory experiments on Dionysos marble can be duplicated in numerical simulations. In this study the rock drilling process is investigated using both the continuum model method, by employing the two-dimensional large-strain explicit finite differences numerical code FLAC^{2D} /3/, and the discrete element code PFC^{2D} /4/.

2. ROCK MICRODRILLING EXPERIMENTS WITH DFTMS

The microdrilling tests were performed with the portable Drilling Force Torque Measurement System (DFTMS) (Fig. 1a,b) which provides continuous measurements of the axial force or weight-on-bit (WOB) and torque (T) on the cutter during the rotational penetration of the drill bit in the stone. During the drilling test the operating conditions are kept constant by pre-specifying the rotational speed (ω) and the penetration rate (v) of the drill bit. The drill bits used for the experiments are coming from the normal masonry practice and are made by soldering a tip of polycrystalline diamond (PCD). The components of this special drilling system dedicated for quasi-non-destructive testing of natural and artificial geomaterials have been reported in a previous paper /5/, however, for easy reference the basic features of DFTMS will be outlined briefly. The system that is illustrated in Fig. 1 consists of:

- *Mechanical Device*: equipped with motors for positioning and drilling.
- *Electronic Unit* : power unit, motor control board for dc motor; motor control board for stepper motor; conditioning amplifier for the load cell signal; graphic display; Keyboard .
- *Tripod*: It can be adjusted in height from 830 to 1600 mm with its legs standing on a plane larger no more than 900 mm in drilling direction. The tripod feet could be fixed to the floor using screws or nails. Its head allows 3D movements in order to correctly positioning the drilling unit.
- *Accessories*: n° 2 steel plates with 3 threaded bars and lock nuts to hold a stone specimen; power line (220 V) and connection cables (serial interface RS232; external power 24 V DC /3A max.); PC's

dedicated software for data elaboration and printing.

The rotation speed of the drill can be set by the user from 0 to 1200 rpm and is controlled by the electronic device (PWM with tacho feedback) *(RS in Fig. 1b)* in order to have a constant speed during the entire drilling work. The displacement of the drill is controlled with a stepper motor to give constant speed of movement with resolution of 0.0025 mm/step. The position of the drill referred to the surface of the stone (starting point) is always known because it is controlled directly by the software through the dedicated electronics. The evaluation of the stone strength parameters are related to the drill penetration force and drilling torque measured by a pair of load cells *(LC in Fig. 1b)*, during drilling. The system measures continuously the penetration force and torque and the actual drill position.

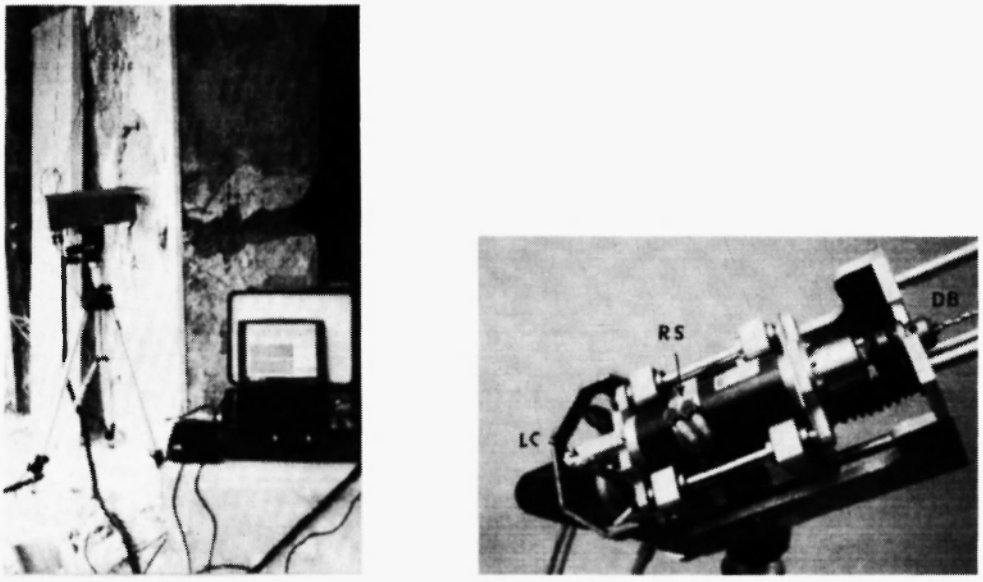

(a) (b)

Fig. 1: (a) In situ drilling tests at a building site with DFTMS, (b) LC=load cell, RS=rotational speed sensors, DB=drill bit.

Several drilling tests (e.g. Table 1) were performed on Dionysos marble in order to measure the drilling thrust and torque reactions on the cutter with respect to the cutting depth δ per revolution that according to basic principles of differential geometry for a circular helix is defined as $\delta = 2\pi v/\omega$

Particular drilling records of force and torque logs corresponding to different cutting depths on a single Dionysos marble specimen of 54 mm diameter and 20 mm height are displayed in Fig. 2 below. It may also be seen in this figure that these primary data have been smoothed by passing the best-fit exponential curve in order to obtain the steady-state values of WOB and T (Table 1).

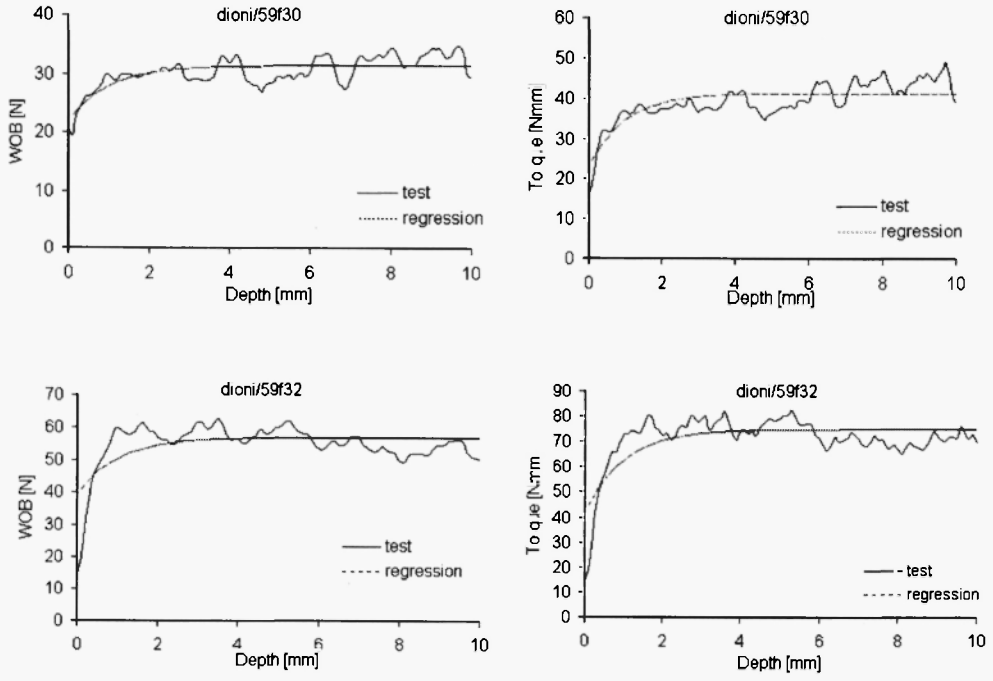

Fig. 2: WOB and torque measurements versus penetration depth on Dionysos marble with a PCD bit of 5mm diameter.

Table 1

Operational parameters and test results of the drilling tests.

Test name	ω /rpm/	v /mm/min/	δ /mm/rev/	WOB /N/	T /Nmm/
DIONI_D59F30	300	1	0.0209	31.38	41.36
DIONI_D59F31	400	4	0.0628	45.66	62.07
DIONI_D59F32	500	8	0.1005	56.88	74.90
DIONI_D59F33	600	10	0.1047	57.87	76.11
DIONI_D59F34	700	15	0.1346	59.87	84.61
DIONI_D59F35	700	15	0.1346	59.87	84.61
DIONI_D59F36	900	20	0.1396	59.83	86.31
DIONI_D59F37	800	10	0.0785	51.35	68.42
DIONI_D59F38	900	15	0.1047	54.83	75.28
DIONI_D59F39	800	15	0.1178	54.85	77.18
DIONI_D59F95	600	10	0.1047	31.34	58.85

Rock cutting experiments on different types of rocks used as monumental stones, such as marbles, limestones and sandstones with uniaxial compressive strengths ranging from 1 MPa to 110 MPa were carried out within the framework of the EU 5th Framework funded Project DIAS /1/. These experiments were performed by using a new portable micro-drilling device that was first designed and constructed for the *in situ* evaluation of the hardness of stones (that is defined as the axial load on the cutter divided by the cross-sectional area of the cut). Subsequently, in a second phase of the tool development, the measurement of torque during drilling was also provided by the manufacturer.

With reference to the conceptual model of the perfectly sharp cutter with a backrake angle θ tracing a groove on a horizontal surface (Fig. 3), a constant ratio μ between the vertical and horizontal components, F_n, F_s respectively, of the force applied to the tool, implies that there is friction on the rock-cutter interface /6/.

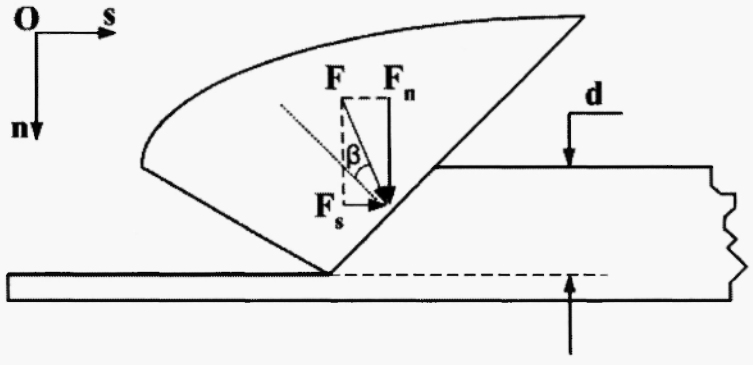

Fig. 3: Sketch of a sharp cutter moving to the left and system of coordinates (F_n=vertical component of cutting force F and F_s=horizontal component)

As may be seen for the graphs of Fig. 4, all $F_n - F_s$ (vertical to horizontal force) diagrams during drilling tests exhibit constant slope μ that seems not to depend on the cutting depth per revolution (i.e. there is no size effect for this type of rock). From this type of elaboration of experimental results the interfacial friction angle of the cutter-rock interface β may be found by virtue of simple geometry as follows

$$\mu = \tan(\theta + \beta) \tag{1}$$

3. A CONTINUUM MODEL OF ROCK CUTTING

For the simulation of the above rock cutting tests we employed the two dimensional large-strain explicit finite differences numerical code FLAC^{2D} version 3.4 by ITASCA /3/. First, the geometry of the cutting face that is prescribed by the geometry of the tool and the cutting depth was properly depicted for the numerical

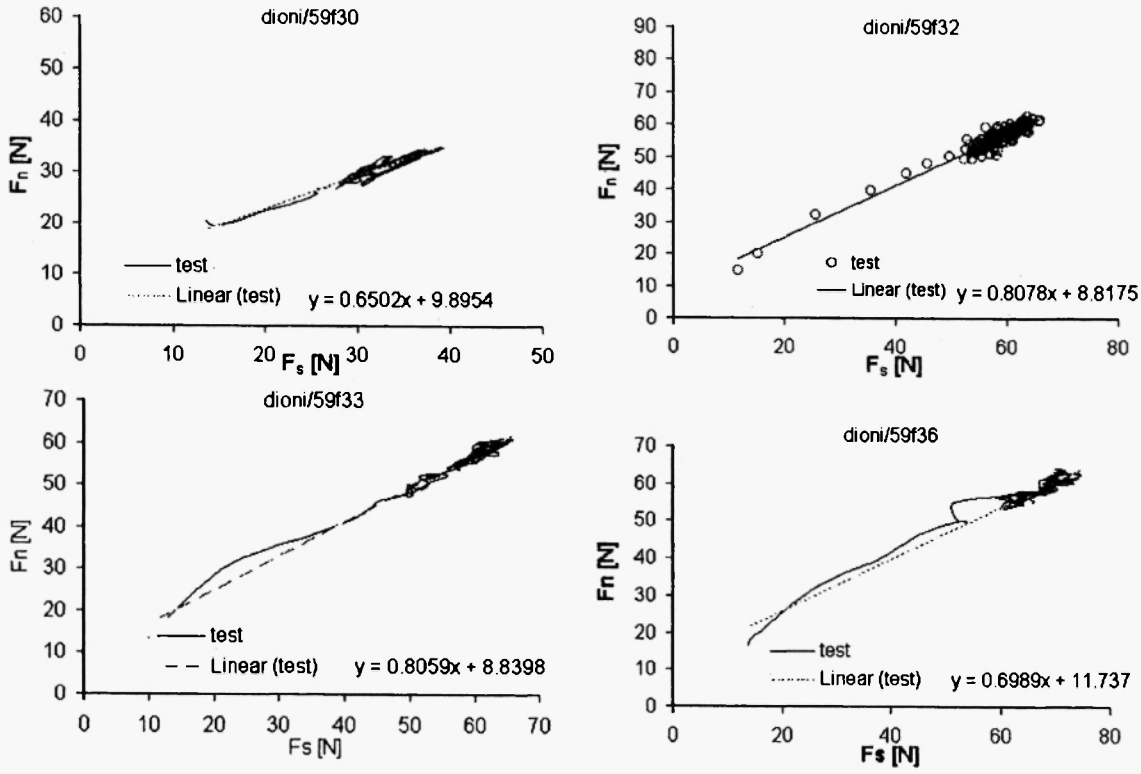

Fig. 4: Determination of inclination angle of vertical vs. horizontal total reaction force acting on the bit.

model. The discretization of the numerical model is dense in the region close to the inclined wall in order to capture the localization process (Fig. 5a). The cutting action (tool-rock interaction) is simulated here by prescribing constant horizontal velocity v to the right of all nodes belonging to the inclined wall (Fig. 5a), whereas the tractions on the horizontal surfaces are prescribed to be zero. The mechanical behaviour of Dionysos marble is approximated by an elastic– perfectly plastic model. For the constitutive law we employ Mohr–Coulomb plasticity, which consists of a yield function f that governs the onset of plastic behaviour $f = \tau + \sigma \sin\varphi - c\cos\varphi$, and a plastic potential function g which describes the flow rule $g = \tau + \sigma \sin\psi - c\cos\psi$, where τ is the maximum shear stress, σ is the mean (hydrostatic) stress. The dilation angle ψ is the ratio of the plastic volume change over the plastic shear strain and is positive for volume increase with increasing shearing strain. For Dionysos marble, the cohesion is c=20 MPa, the maximum angle of internal friction is φ = 40°, the dilatancy angle is assumed to be zero , the modulus of elasticity is E=80 GPa and Poisson's ratio $\nu = 0.33$ /1/. The distorted finite difference grid, as well as contours of maximum shear strain rate corresponding to successive amounts of sliding u along the horizontal plane are illustrated in Fig. 5.

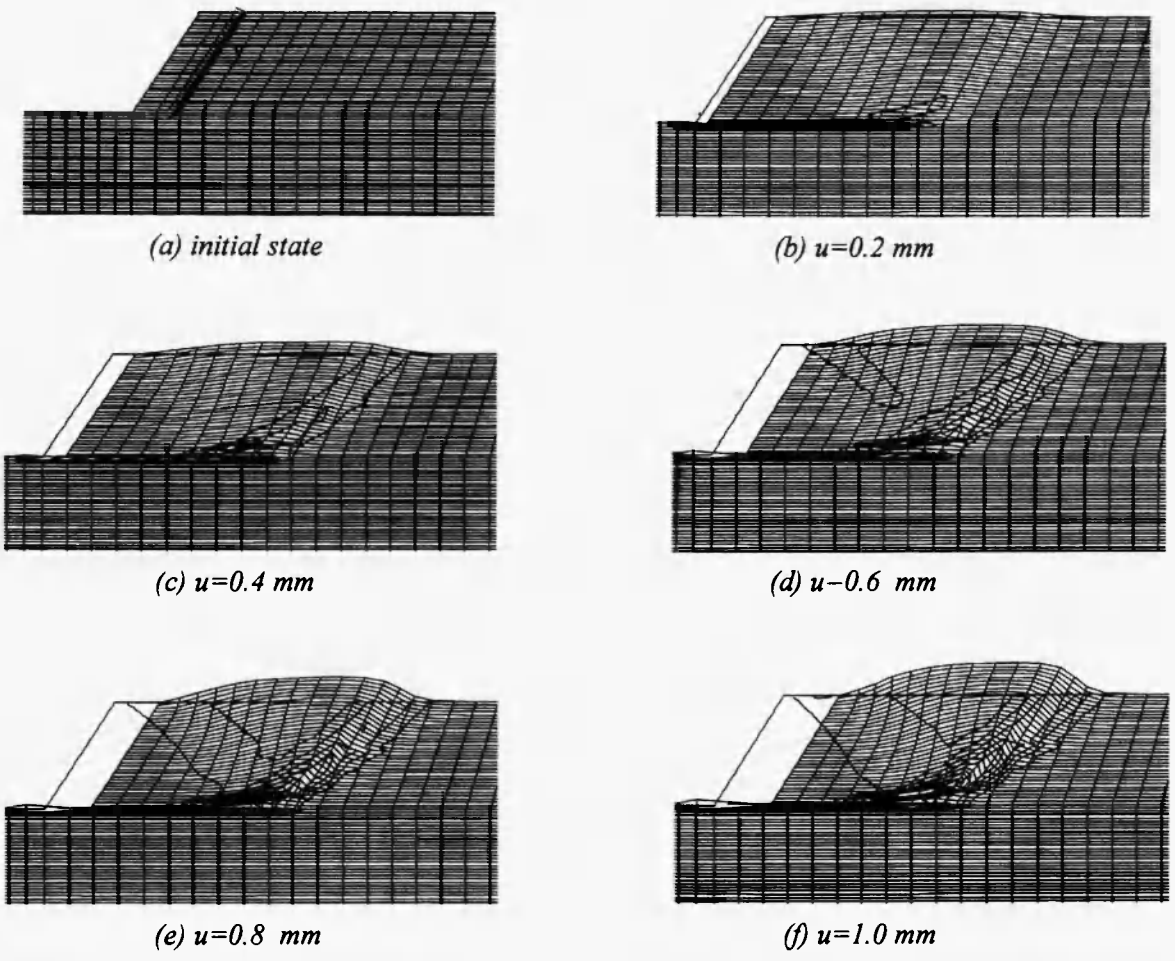

Fig. 5: (a) Initial state of the model, and (b,c,d,e,f) exaggerated deformed grid and contours of maximum shear strain in rock cutting simulation with FLAC^{2D} (cutting depth δ = 0.1mm).

Several numerical models have been simulated in order to study the influence of the cutting depth δ on the force-displacement behavior of the tool. Fig. 6 displays the variation of the horizontal and vertical components of the thrust force acting on the cutter with the horizontal displacement.

Subsequently, the mean values of horizontal and vertical cutter forces calculated for the various simulated cutting depths have been plotted in Fig. 7. In the same figure the measured cutting forces by DFTMS in the laboratory are also displayed for comparison purposes. Interestingly model predictions are in very good agreement with the drill cutting measurements on the Dionysos marble specimen. It may also be noted that cutting forces are proportional to the cutting depth for this type of stone.

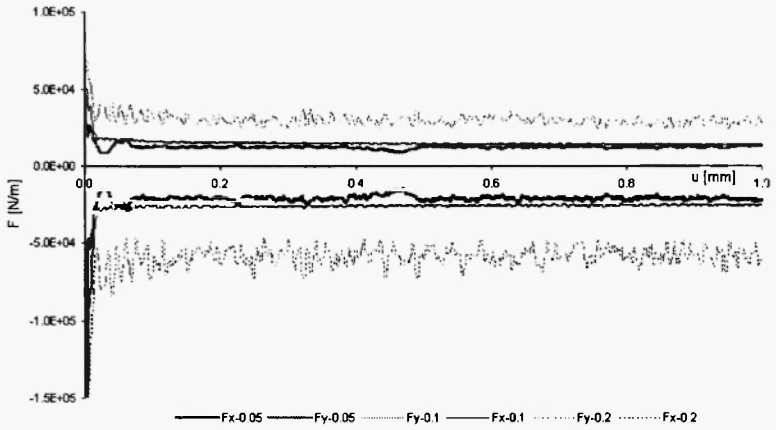

Fig. 6: Plots of $F_y - F_x$ vs. tool displacement for the various cutting depths at hand ($\delta = 0.05, 0.1, 0.2$ mm).

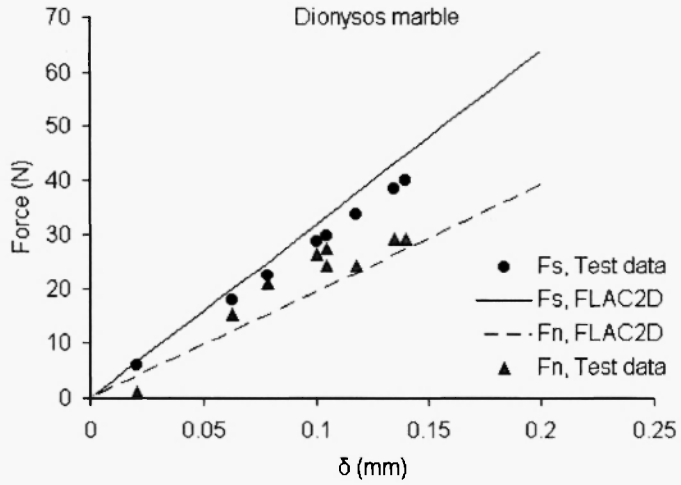

Fig. 7: Plots of measured and predicted forces vs. cutting depth

4. A MICROMECHANICAL DISCRETE ELEMENT MODEL OF ROCK CUTTING

Rock cutting simulations have been performed by using the discrete element method. For this purpose the numerical code PFC^{2D} (Particle Flow Code of 2 Dimensions) /4/ has been employed to model the PCD bit as a set of walls, that moves at a specified horizontal velocity and depth of cut on a horizontal surface of a granular rock while monitoring traction forces applied on the cutter and damage in the rock.

PFC^{2D} is used to simulate the behavior of a type of marble (Dionysos marble), under different conditions of rotary drill cutting. Those conditions mainly correspond to cutting depth as the geometry of the cutter resembles that of the microdrilling device, the material behavior matches that of Dionysos marble, and the cutter is moved slow enough in order to approximate quasistatic loading conditions. PFC^{2D} models solids as a

collection of distinct and arbitrarily sized circular particles. In order to setup a model three fundamental components of the model must be specified:

1. *The assembly of particles:* It consists of the locations and *size distribution* of particles (circular discs) (Fig. 8).
2. *The contact behavior and material properties of the assembly:* They dictate the type of response the model will exhibit upon disturbance (e.g. deformation response due to biaxial loading).
3. *The boundary and initial conditions:* The initial *in-situ* stress state of the model before any disturbance is introduced into the model.

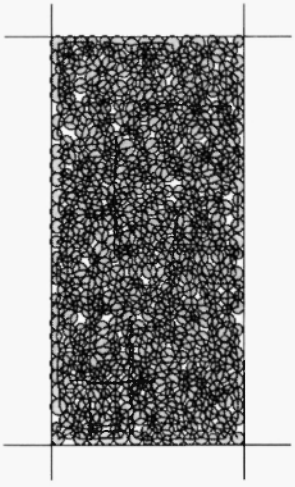

Fig. 8: Assembly of 540 particles (circular discs) confined between servo-controlled smooth walls for the simulation of a biaxial test and bonds (lines) between the balls

The motion and the interaction of the rigid particles in PFC^{2D} code are established by the following three sets of parameters:

(a) Geometric and physical parameters:

$\bar{R}$ $[L]$ = average ball radius

ρ $[F \cdot L^{-4} \cdot T^2]$ = density of particles

n $[-]$ = porosity of the particle assembly

(b) Micromechanical parameters for the contacts between the particles:

K_n $[F \cdot L^{-2}]$ = contact normal stiffness

K_s $[F \cdot L^{-2}]$ = contact shear stiffness

$E_c = \frac{K_n}{2} = \frac{K_s}{2}$ $[F \cdot L^{-2}]$ = ball-ball contact modulus

T_n $[F \cdot L^{-1}]$ = contact-bond normal strength

T_s $[F \cdot L^{-1}]$ = contact-bond shear strength

$\sigma_c = \frac{T_n}{2 \cdot R}$ $[F \cdot L^{-2}]$ = material normal strength

$\tau_c = \frac{T_n}{2 \cdot R}$ $[F \cdot L^{-2}]$ = material shear strength

μ [–] = friction coefficient

(c) Loading condition parameters:

L $[L]$ = characteristic dimension of the model

v $[L \cdot T^{-1}]$ = applied wall velocity

The contacts between particles are described through the stiffness, slip condition, and bonding models. Herein a linear force-displacement constitutive law at each contact is assumed, namely

$$F_n^i = K_n \cdot U_n^i \cdot n_i, \quad \Delta F_s^i = -K_s \cdot \Delta U_s^i \tag{2}$$

where F_n^i, F_s^i are the normal and shear components of the contact force; U_n^i, U_s^i are the displacement components along the normal and tangential directions of the contact, respectively. Further a linear Coulomb-type failure criterion at the ball contacts has been adopted

$$F_n^i = F_s^i = 0 \quad \text{if} \quad F_n^i > T_n, \quad \left|F_s^i\right| = \mu \cdot \left|F_n^i\right| \quad \text{if} \quad F_s^i \geq T \tag{3}$$

The next step is to quantify the micromechanical model parameters in order to duplicate as close as possible the mechanical properties of Dionysos marble measured or inferred from laboratory standard tests (see Appendix A). Since there are no relationships that connect these two sets of parameters (i.e. micromechanical with macromechanical) a number of 2D uniaxial compression simulations have been performed. The results of this study, pertaining to the dependence of Young's modulus (E') and the Poisson's ratio (ν') are shown in Fig's 9 a,b below.

Since the distinct element code is two-dimensional it may be interpreted as representing either a plane stress or plane strain condition. Herein, plane strain conditions are assumed hence the two-dimensional constants E' and ν' can be related to E and ν according to the relations

$$E' = \frac{E}{1-\nu^2}, \quad \nu' = \frac{\nu}{1-\nu} \tag{4}$$

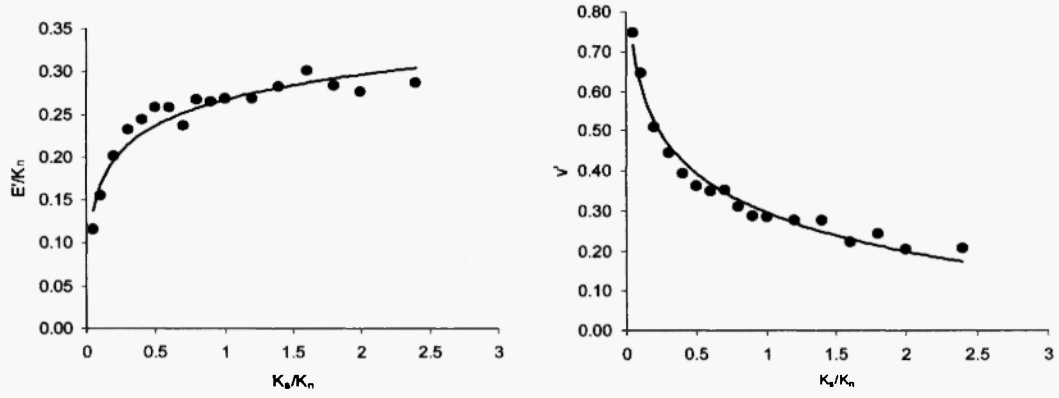

(a) *(b)*

Fig. 9: (a) Apparent Young's modulus, and (b) apparent Poisson's ratio as a function of the stiffness ratio K_s/K_n

Based on the above phenomenological relationships in dimensionless form, the set of micromechanical properties has been found (Table 2), that gives the best possible comparability between the model with the uniaxial and triaxial compression experimental tests. Fig. 10a shows the distribution of the contact forces inside the specimen that is subjected to unconfined compression. Further, Fig's 10 b,c display the comparison of model predictions and test results pertaining to the axial stress vs. axial strain and lateral strain vs. axial strain behavior.

Table 2

Properties of the contact bonded material micromechanical model

Property	**Symbol**	**Numerical value**
Ball density (kg/m3)	ρ	2700.00
Ball-ball contact modulus (Pa)	E_c	1.25E+11
Ball stiffness ratio	K_n/K_s	2.00
Ball Normal stiffness (N/m)	K_n	2.50E+11
Ball friction coefficient	μ	0.50
Contact bond normal strength (Pa), mean	σ_c	5.50E+07
Contact bond normal strength (Pa), std.dev.	σ_c	1.00E+07
Contact bond shear strength (Pa), mean	τ_c	4.50E+08
Contact bond shear strength (Pa), std. dev.	τ_c	1.00E+07

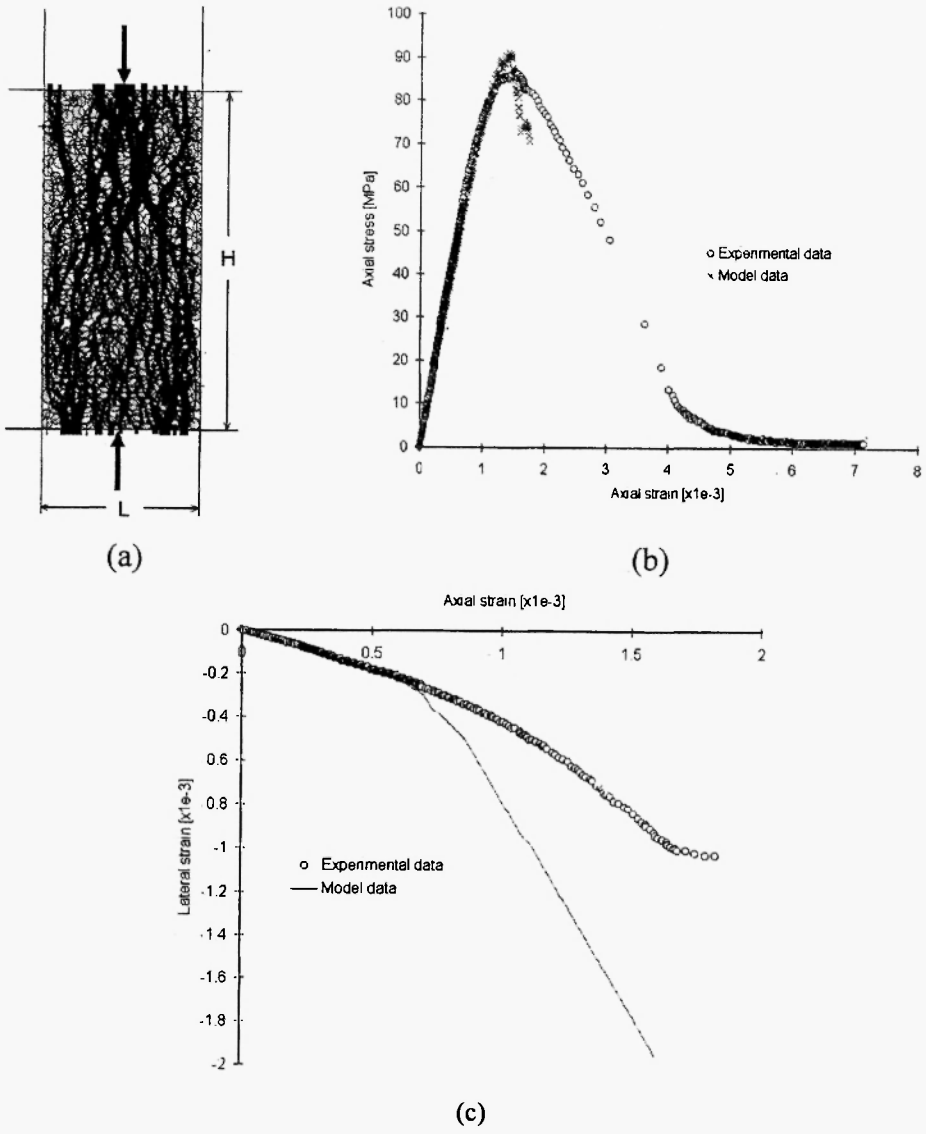

Fig. 10: 2D simulation of uniaxial compression test with H/L=2; (a) distribution of contact forces inside the specimen during compression (thickness proportional to magnitude), (b) axial strain-axial stress curves, and (c) predicted and measured axial strain-lateral strain curves

A series of triaxial compression tests on the same rectangular disc assembly simulating the rock specimen have been also simulated in order to verify that the bond strength parameters adopted in this work (Table 2) result to good comparability with experimental data. The good agreement of the model with experiments is illustrated in Fig. 11.

From Fig. 10c it may be noted that the distinct model overestimates Poisson's ratio above some axial strain level whereas underestimates rock strength above a certain confining stress (due to somewhat lower friction angle of the grain packing model) (Fig. 11).

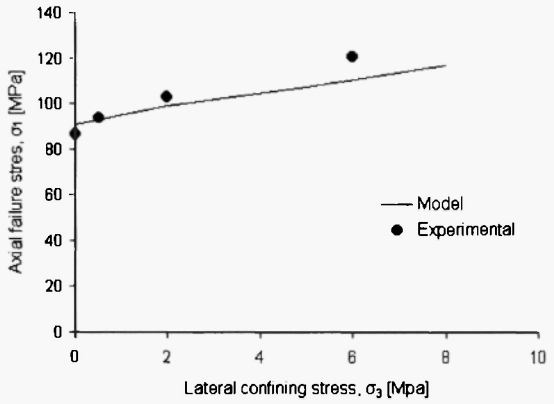

Fig. 11: Comparison of Dionysos marble triaxial test strength results and calibrated model predictions in principal stress (σ_1, σ_3) space

Next, the calibrated granular model is used for the simulation of the rock cutting tests. Typical numerical results pertaining to the variation of cutting forces with sliding distance of the cutter that correspond to a small and a large cutting depth, respectively, are displayed in Figs. 12 and 13.

Further, the dependence of the mean values of the horizontal force (over the distance traveled by the sharp cutter) on the dimensionless cutting depth predicted by the micromechanical model is shown in Fig. 14. The best possible agreement of the continuum model results with the discrete model predictions permits the estimation of the mean particle radius $\overline{R}$. From this analysis the best-fit value of the mean grain radius has been found to be $\overline{R} = 300\ \mu m$ which is not very far from the mean grain radius of this marble that is of the order of $200\ \mu m$ /1/.

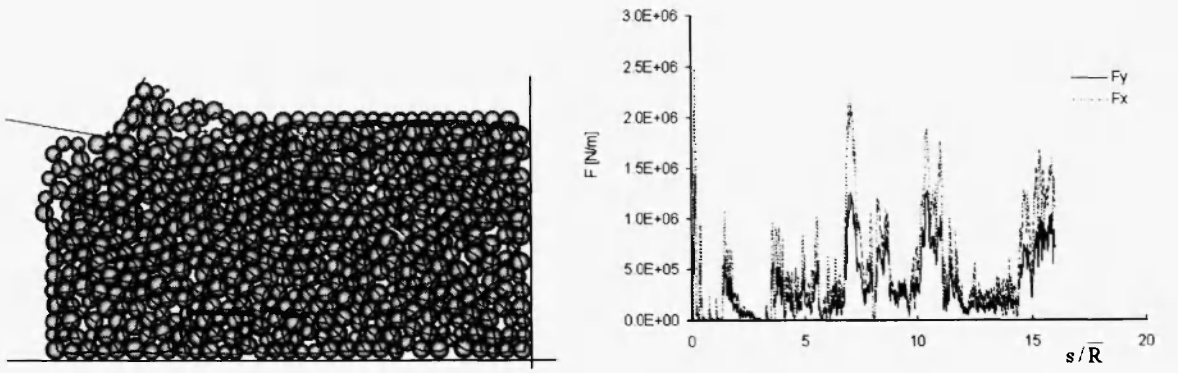

(a) (b)

Fig. 12: (a) Distorted granular fabric due to tip motion to the right and damage close to the cutter tip (at time step 24000), (b) force vs. distance plots for the case $\delta / \overline{R} = 3$

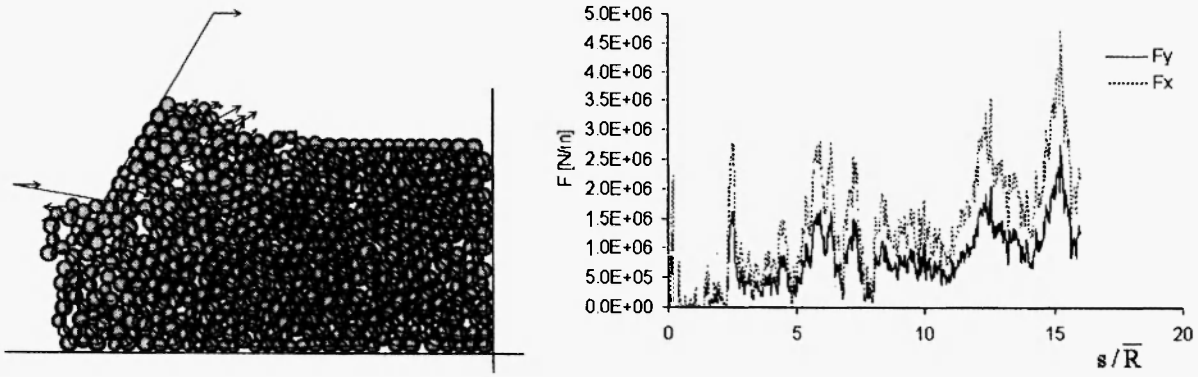

(a) (b)

Fig. 13: (a) Granular fabric and damage close to the cutter tip (at time step=25000) and (b) force vs. distance plots for the case $\delta / \bar{R} = 9$

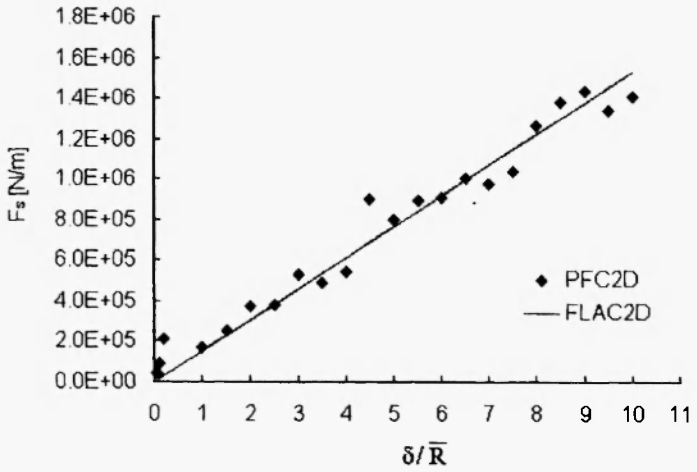

Fig. 14: Variation of mean horizontal force with the relative depth of cut predicted by the two models

5. CONCLUSIONS

The main conclusions of our study are:

a) Continuum calculations of Dionysos marble cutting done with an elastic-perfectly plastic model with a non-associated flow rule are in good agreement with experimental results.

b) The micromechanical distinct element calculations duplicate continuum model predictions for a mean grain size of $\bar{R} = 710\,\mu m$. This value is not very far from the mean grain radius of this marble that is of the order of 200 μm. According to fundamental principles of fracture mechanics the mode-I fracture toughness is given as $K_{IC} = \sigma_t \sqrt{\pi \bar{R}}$. For the value of uniaxial tensile strength of marble, $\sigma_t = 35$ MPa, found by micromechanical calculations in Brazilian disc configuration, it may be found that $K_{IC} = 1.7\ MPa\sqrt{m}$ and the specific fracture energy $2\gamma = K_{IC}^2 / E = 34.16\ J/m^2$.

ACKNOWLEDGEMENTS

The authors are grateful for the financial support from the EU 5th Framework Project "Integrated tool for in situ characterization of effectiveness and durability of conservation techniques in historical structures" (DIAS) with Contract Number: DIAS-EVK4-CT-2002-00080.

6. REFERENCES

1. G.E. Exadaktylos, I[st] Year Report on "*Integrated tool for in situ characterization of effectiveness and durability of conservation techniques in historical structures*", Technical University of Crete (2004).
2. P. Tiano, C. Filareto, M. Ferrari, S. and C. Ponticelli and E. Valentini, Drilling Force Measurement System, a new standardizable methodology to determine the "Superficial Hardness" of monumental stones: Prototype design and validation, *International Zeitschrift fur Bauinstandsetzen und Baudenkmalpflege 6*. Jahrgang, Aedificatio Publishers, **2**, 115-132 (2000).
3. ITASCA, *Fast Lagrangian Analysis of Continua (FLAC) User's Guide*, Itasca Consulting Group, Minneapolis, Minnesota (1998).
4. ITASCA, *Particle Flow Code in 2 dimensions, PFC[2D] User's Guide*, Itasca Consulting Group Inc., Minneapolis, Minnesota (2002).
5. G. Exadaktylos, P. Tiano, and C. Filareto, Validation of a model of rotary drilling of rocks with the drilling force measurement system. *International Zeitschrift fur Bauinstandsetzen und Baudenkmalpflege 6*. Jahrgang, Aedificatio Publishers, **3**, 307-340 (2000).
6. E. Detournay and P. Defourny, A phenomenological model for drilling action of drag bits, *Int. J. Rock Mech. Min. Sci. & Geomech. Abstr.*, **29** (1): 13-23 (1992).

APPENDIX A
Standard physico-mechanical properties of Dionysos marble

This type of marble consists of an equidimensional mosaic of fine calcite grains with straight to gently curved boundaries having an average size of 400 μm. Its mineralogical composition by weight is calcite = 98%, quartz = 0.5%, muscovite = 0.5%, sericite = 0.5%, chlorite = 0.5%; some small percentage of dolomite may be also present in its composition. It has a unit weight of 2.67 (x 10^5 N/m^3), porosity 0.371%, and absorption coefficient by weight 0.11%. The microscopic petrographical images with parallel and crossed Nicols of Dionysos marble are illustrated in Fig. A.1.

Fig. A.1: Typical optical micrographs of Dionysos marble taken with crossed Nicols. Uniaxial compression test results

In this work we employ a database of uniaxial compression experiments on Dionysos marble specimens with diameter D=5 cm and height H=10 cm. In all the tests carried out in the frame of this work a certain number of unloading-reloading cycles were performed in order to study the elasticity of the test specimens. During its test the axial force (F), the engineering axial strain (ε_a) and the engineering radial or lateral strain (ε_ℓ) were monitored and stored in a worksheet for further elaboration. The graphs of axial stress vs. axial, lateral and volumetric strains, and lateral strain vs. lateral strain referring to Dionysos marble loaded perpendicularly to the plane of transverse anisotropy are displayed in Figs A.2a and A.2b, respectively.

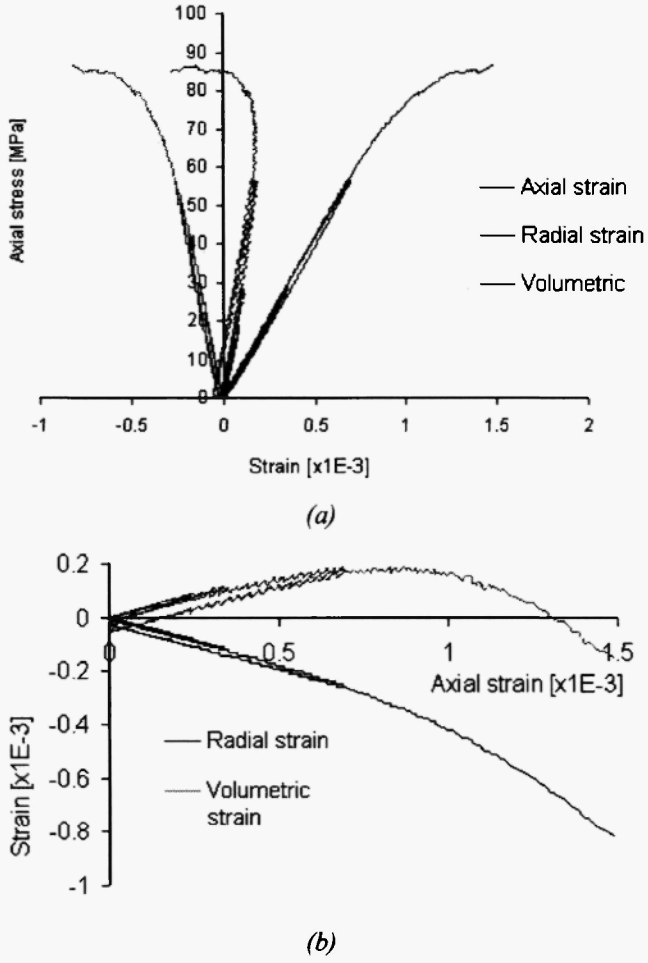

Fig.A.2: Typical (a) axial stress vs. axial, radial and volumetric strains, and (b) volumetric and lateral strain vs. axial strain curves of Dionysos marble.

For the cylindrical samples subjected to axial loading and under small strains the volumetric strain (ε_v) is computed by the formula

$$\varepsilon_v = (2\varepsilon_\ell + \varepsilon_a) \tag{A.1}$$

The data taken from primary loading loops are fitted by polynomials of the form

$$\begin{aligned} \sigma_a &= a_1 x + a_2 x^2 + a_3 x^3 + \ldots, \\ 1000 \cdot \varepsilon_\ell &= b_1 x + b_2 x^2 + b_3 x^3 + \ldots, \\ x &= 1000 \cdot \varepsilon_a \end{aligned} \tag{A.2}$$

The nonlinearity of NB stones is manifested by the dependence of the tangent (or secant) modulus of elasticity and lateral strain factor on the applied stress. In fact, differentiating (2) with respect to ε_a we obtain

$$E_t = \frac{\partial \sigma_a}{\partial \varepsilon_a} = a_1 + 2a_2 x + 3a_3 x^2 + ...,$$
$$\nu_t = -\frac{\partial \varepsilon_l}{\partial \varepsilon_a} = -b_1 - 2b_2 x - 3b_3 x^2 + ... \qquad \text{(A.3)}$$

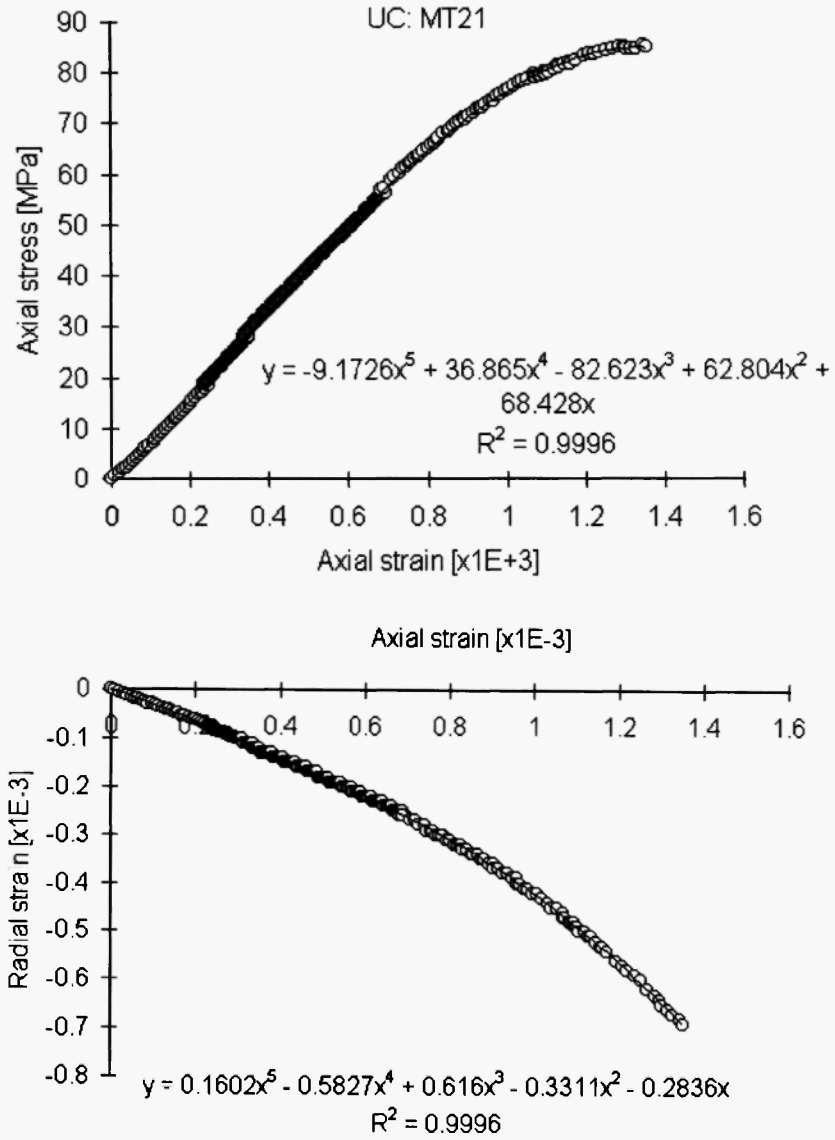

Fig. A.3: Loading branches of (a) axial stress- axial strain and (b) lateral strain-axial strain curves of Dionysos marble in UC and fitted polynomial curves.

The experimental parameter a is identified here as the initial tangent modulus of elasticity denoted by the symbol E_i.

However, the elastic constants of a material are determined from the unloading-reloading branches during a cyclic compression experiment. From Fig. A.4 below we observe that the mechanical behavior of marble during unloading and reloading is nonlinear and hysteretic. In fact, hysteresis is manifested by different paths during unloading and reloading, whereas plastic deformation – due to internal stone damage - is manifested by permanent axial strain after complete unloading. Further, the width of the loops increases with increasing axial stress where unloading is performed. In the frame of a simple isotropic elasto-plastic theory the data processing will give the two elastic constants. For this purpose we interpolate the best linear curve through each loop from the slope of which we calculate the two elastic constants.

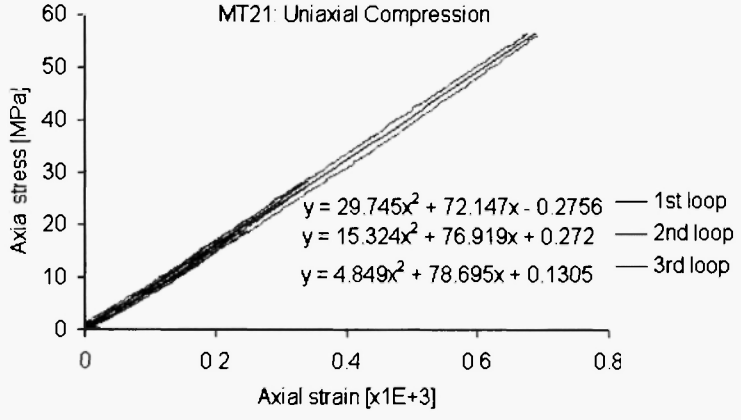

(a)

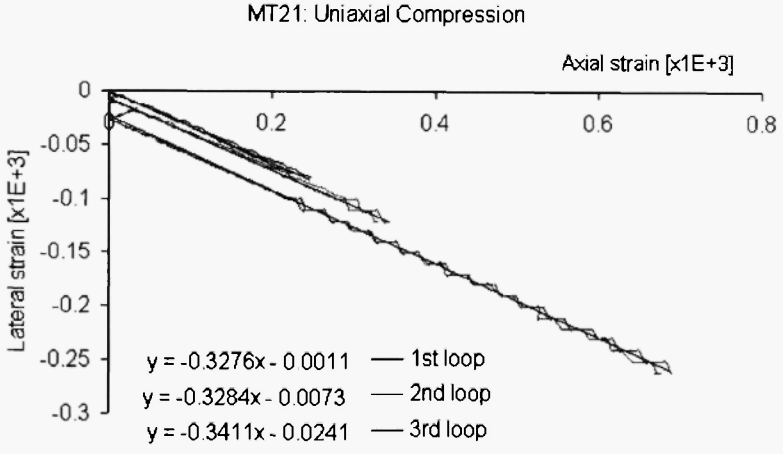

(b)

Fig. A.4: Unloading-reloading loops of Dionysos marble in uniaxial compression.

From Fig. A.5 it can be seen that both elastic moduli of this type of marble remain constant during the unconfined compression test.

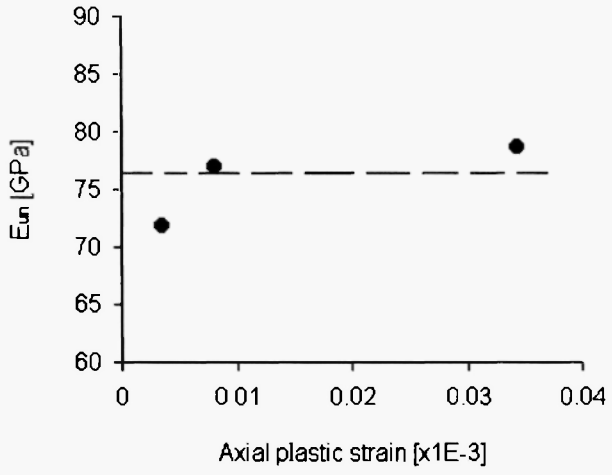

(a)

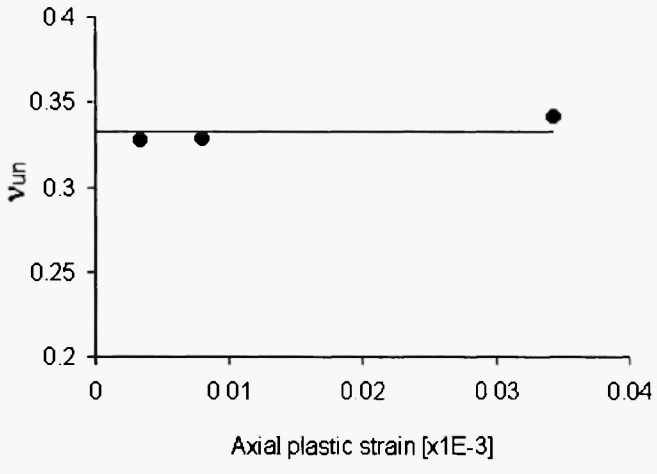

(b)

Fig. A.5: Variation of (a) Young's modulus and (b) Poisson's ratio with axial plastic strain of Dionysos marble in uniaxial compression